Satellite-based measurements of surface deformation reveal fluid flow associated with the geological storage of carbon dioxide

D. W. Vasco[1], Alessio Rucci[2], Alessandro Ferretti[3], Fabrizio Novali[3], Rob Bissell[4], Philip Ringrose[5], Allan Mathieson[4], and Iain Wright[4]

[1]Earth Sciences Division, Lawrence Berkeley National Laboratory, Berkeley; [2]Politecnico di Milano, Milano, Italy; [3]Tele-Rilevamento Europa-TRE, Milano, Italy; [4]BP Alternative Energy, Middlesex UK
[5]StatoilHydro Research Centre, Trondheim, Norway

Interferometric Synthetic Aperture Radar (InSAR), gathered over the In Salah CO_2 storage project in Algeria, provides an early indication that satellite-based geodetic methods can be effective in monitoring the geological storage of carbon dioxide. An injected volume of 3 million tons of carbon dioxide, from one of the first large-scale carbon sequestration efforts, produces a measurable surface displacement of approximately 5 mm/year. Using geophysical inverse techniques we are able to infer flow within the reservoir layer and within a seismically detected fracture/ fault zone intersecting the reservoir. We find that, if we use the best available elastic Earth model, the fluid flow need only occur in the vicinity of the reservoir layer. However, flow associated with the injection of the carbon dioxide does appear to extend several kilometers laterally within the reservoir, following the fracture/fault zone.

1. Introduction

The geological storage of carbon dioxide (CO_2) is likely to be an important tool for preventing greenhouse gases from entering the atmosphere [Baines and Worden, 2004; Schrag, 2007]. This approach involves injecting large quantities of carbon dioxide underground using one or more deep boreholes. However, in order for such storage to be safe and effective, the CO_2 must remain at depth. Past experience with the use of CO_2 for secondary oil recovery suggests that the migration of carbon dioxide within the Earth can be complicated, and can differ from the movement of injected water or the flow of hydrocarbons [Lazaratos and Marion, 1997; Hoversten et al., 2003; Arts et al., 2004; White et al., 2004]. Due to the complexity of the movement of carbon dioxide within the Earth, and the desire to keep this greenhouse gas from migrating towards the surface and eventually reaching the atmosphere, there is a need to monitor the fate of the injected CO_2.

In many important settings, satellite-based geodetic techniques can fulfill the twin goals of long-term, cost-effective monitoring [Massonnet and Feigl, 1998; Burgmann et al., 2000]. Satellite-based surveillance can be less expensive, more frequent, and less invasive than other geophysical monitoring techniques such as seismic or electromagnetic methods. On dry land, Interferometric Synthetic Aperture Radar (InSAR) can provide high spatial resolution (a few meters or tens of meters) and almost monthly measurements of surface deformation. Roughly speaking, InSAR utilizes the phase change of radar reflections off the Earth's surface to measure minute changes in the position of the reflection points [Massonnet and Feigl, 1998; Burgmann et al., 2000]. Given the presence of radar reflectors of suitable quality, InSAR can be used to detect surface motion with an accuracy of a few millimeters. In this fashion, InSAR has contributed significantly to the intermediate and long-term monitoring of ground motion associated with numerous phenomena, such as groundwater variations, geothermal production, earthquake-related strain, tunneling and mining, and oil and gas production [Massonnet and Feigl, 1998; Burgmann et al., 2000]. We should note that geodetic monitoring, as described here, can be extended to offshore fields through the use of precision seafloor gravity and pressureobservations [Zumberge et al., 2008; Alnes et al., 2008] or possibly through the use of interferometric synthetic aperture sonar [Chang et al., 2000; Hansen et al., 2006].

2. The In Salah CO_2 Storage Project

We utilize InSAR observations gathered over a site of active CO_2 storage to image ground motion induced by the injected fluid volume. The injected carbon dioxide is associated with the In Salah CO_2 storage project located in Algeria [Vasco et al., 2008; Ringrose et al., 2009], one of only two existing large-scale sequestration efforts, the other being the Sleipner field under the North Sea [Arts et al., 2004]. In addition, there are projects in which carbon dioxide is injected into partially depleted oil reservoirs as a means of sequestration as well as enhancing oil recovery, as in the Weyburn project in Canada [White et al., 2004]. The In Salah project, which has been operational since 2004, gathers excess carbon dioxide that is present in natural gas extracted from three adjacent gas fields. The carbon dioxide is compressed, dehydrated, and transported to three horizontal wells, where it is injected into a 1800 to 1900 m deep saline formation, down-dip of the gas fields. The target formation for the storage of the CO_2 is twenty meters of Carboniferous sandstone with approximately 15% porosity and an estimated permeability of 10 mD [Ringrose et al., 2009]. The sandstone formation is part of a northwest trending anticline that defines the natural gas field. The reservoir is overlain by more than a kilometer of interbedded shales which act as a barrier to flow. From 2004 to 2008 over 3 million tons of CO_2 have been injected into the formation. The project has a planned life-span of more than 20 years.

3. Satellite-Based Monitoring

Following the initiation of injection at In Salah, Tele-Rilevamento Europa (TRE) and Lawrence Berkeley National Laboratory acquired, processed, and analyzed satellite radar images from the European Space Agency's (ESA)

Envisat archive [*Vasco et al.*, 2008] in order to evaluate InSAR's potential for monitoring the fate of the injected CO_2. Two satellite paths, Track 65 and Track 294, repeatedly passed over the In Salah site, providing an irregular time sequence of 41 radar reflection images from July 12, 2003 through March 19, 2007 [*Vasco et al.*, 2008]. The data associated with each satellite pass consists of a Frame, a dense grid of 20 m by 20 m pixels, covering an area of 100 km by 100 km. In our analysis we examine the backscattered radar signal and identify permanent scatterers [*Ferretti et al.* 2001]. These are objects at the Earth's surface, a subset of the pixels within the Frame, some 300,000 in all, which return stable reflections for a given time sequence of radar images (Figure 1).

Once the permanent scatterers are identified we construct corrections for atmospheric and orbital effects and derive a time series for changes in the distance between a reference point in space and the scatterers located on the Earth's surface [*Ferretti et al.*, 2001]. Such range changes observations provide a measure of the displacement of the Earth's surface. For example, Figure 1 is an image of the range velocities, in mm/year, of the 300,000 permanent scatterers over the more than three years of injection. The individual radar images are spaced roughly one to three months apart in time and provide a time series of the surface deformation associated with the CO_2 injection [*Vasco et al.*, 2008]. The velocities in Figure 1 are computed by estimating the slope of a line fit to the range change time series of each permanent scatterer. In Figure 1 there are observable decreases in range, of the order of 5 mm/year, associated with the three injection wells, corresponding to uplift. Note the variations in the pattern of range change over the labeled injectors in Figure 1. For example, the range decrease over well KB-501 is elongated in a north-northwesterly direction, suggesting preferential flow. Above injection well KB-502 there are two lobes of range decrease, a pattern characteristic of the opening of a tensile feature such as a fault or fracture [*Davis*, 1983]. In addition to the range decreases over the injectors, there are range increases associated with subsidence due to gas production and subsidence associated with the various stream beds (ephemeral wadis) in the region.

4. Estimation of Reservoir Volume Change and Fault/Fracture Aperture Change

Given the estimates of deformation provided by the InSAR data (Figure 1), our aim is to relate the ground motion to flow-related processes at depth. This is an example of an inverse problem in which observations made at the surface of the Earth are used to infer processes or properties at depth [*Vasco et al.*, 2000]. We restrict our attention to an analysis of the two-lobed pattern of surface deformation above injector KB-502 (Figure 1). Injection started in April 2005 at a rate of over 280,000 cubic meters of CO_2 per day [*Ringrose et al.*, 2009]. Shortly afterward, the ground above the well began to rise at a rate of about 5 $mm/year$. As noted above, the two-lobed pattern of deformation evident in the range velocity estimates (Figure 1), is suggestive of the opening of a tensile feature at depth [*Davis*, 1983]. The existence of such a fault/fracture is supported by data from a seismic reflection survey and by logging information from well KB502 [*Ringrose et al.*, 2009]. The fault/fracture is thought to be vertical or dip at a very high angle and to lie between the two lobes of range decrease, trending to the northwest. The exact vertical extent of the fault/fracture is not well constrained but it does intersect the reservoir interval. Because the reservoir is bounded above and below by lower permeability formations and contains natural gas, we expect that the twenty meters of Carboniferous sandstone comprising the reservoir will provide a stable conduit for the migration of the injected CO_2. Due to these considerations we construct a model containing two components: the opening (aperture change) of an extended tensile feature representing a fault or a fracture, and volume change within the 20 m thick reservoir interval.

4.1. The Importance of an Accurate Elastic Earth Model

Using logs from several wells in the area we are able to construct a 20-layer model of compressional and shear velocity for the region (Figure 2a). A numerical code is used to compute the displacement fields in this layered model [*Wang et al.*, 2006]. The reservoir, which lies at a depth of around 1.8 km, is situated in a low velocity zone (Figure 2a). This fact turned out to have a significant impact on the calculated surface deformation associated with a given tensile source.

An example calculation shows that the opening of a vertical tensile crack in a low velocity zone produces range velocity variations which are significantly different from those associated with a homogeneous half-space (Figure 2b). In the example shown in Figure 2, the fracture lies at the reservoir depth of 1.8 km, is 4 km long, and 100 m in vertical extent and opens by 5 cm. The fault/fracture model is presented here for illustration only, to demonstrate the influence of a low velocity zone upon deformation at the Earth's surface, and is not intended to represent a realistic source model. Therefore, the exact values of the fault/fracture length, which were roughly estimated from the length of the anomaly in Figure 1, and the width, which is was taken arbitrarily, are not critical. In Figure 2b we plot the range velocity along a line transverse to the plane of the tensile crack. Range velocities were computed for two elastic models: a uniform half-space and the layered model (Figure 2a). While both models display the characteristic two-lobed pattern of a tensile fracture, the range change for the uniform elastic model (Uniform moduli) is very different from that of a 20 layer elastic model (Layered moduli). The height and spacing of the lobes varies notably for the two models and the uniform model has a significant peak that is not present in the layered model. As an aside, we note that the bi-lobed pattern in Figure 2b is asymmetric because range change is not equivalent to the vertical displacement. Rather, range change is a projection of the displacement vector onto a vector that points from the observation point to the location of the satellite in space [*Burgmann et al.*, 2000]. The fact that the variation of elastic properties with depth can influence the surface deformation for a given source model has been noted by others [*Chinnery and Jovanovich*, 1972; *Savage*, 1987; *Hearn and Burgmann*, 2005]. However, the dramatic change when a tensile source lies within a low velocity zone (Figure 2b) surprised us and does not appear to be cited in the literature.

4.2. Inverting the Range Change Estimates

Having settled upon the major constituents of our source model and the elastic structure of the overburden, we now solve the inverse problem. That is, we use the range change observations to obtain estimates of the reservoir volume change and the opening of the fault/fracture. The reservoir layer geometry is fixed by the position of its boundaries, determined by 3D seismic data [*Ringrose et al.*, 2009]. The overall characteristics of the planar fault/fracture are determined from the range change observations themselves. We find that a vertical fault/fracture model provides a good fit to the range changes. The final geometry of the

fault/fracture model is indicated in Figure 3. In the upper-panel of this figure we plot the northwest trending surface trace of the vertical fault/fracture.

Both the reservoir layer and the fault/fracture plane are sub-divided into 8 by 8 grids of cells which can undergo fractional volume change or aperture change, respectively. Aperture change is opening of the fracture due to the injected fluid volume, while the fractional volume change is the volumetric expansion of the porous sandstone comprising the reservoir interval. We extend the fault plane above and below the reservoir center line by 80 m in order to model any possible vertical propagation of this feature. Because we shall allow for a spatial distribution of fault/fracture aperture changes, the exact vertical boundaries are not critical, so long as our grid is large enough to contain all significant aperture change. An iterative least squares solver is used to find the reservoir layer volume expansions and the fault/fracture plane aperture changes which best fit the range change observations. The overall approach is similar to that described in Vasco et al. (2000).

The resulting fault/fracture plane aperture changes and reservoir fractional volume changes are shown in Figure 3. The fractional volume changes in the upper panel (Figure 3a) indicate that flow within the reservoir layer was confined to the region immediately surrounding the injection well. The aperture changes on the fault/fracture plane are shown in the lower panel (Figure 3b), suggest that the fluid has migrated several kilometers to the northwest, 40 m above and below the reservoir. Thus, the fault/fracture zone appears to be acting as a high conductivity pathway for the injected fluid. Note that the fractional volume (Figure 3a) and aperture changes (Figure 3b) relate fundamentally to pressure changes and do not necessarily indicate the exact location of the CO_2. That is, the pressure changes are associated with flow in the formation and are not confined to regions of saturation change. As indicated in Figure 4, using the two-component model shown in Figure 3, we are able to fit the overall features of the range velocity data including the two-lobed pattern.

5. Conclusions

This study illustrates that satellite-based observation can provide an effective approach for monitoring the fate of carbon dioxide injected deep within the Earth. The injected volume of CO_2, associated with one of the few large-scale sequestration efforts currently under way, gives rise to a measurable surface deformation of a few millimeters per year. The dense spatial sampling provided by the InSAR data suggests preferential flow away from the injection wells and evidence of the opening of an existing tensile feature. The tensile feature coincides with a seismically imaged fault intersecting the reservoir. The fault/fracture model most likely represents the dilation of a network of fractures or an extended fault zone, rather than a single fracture. The aperture change is then indicative of the cumulative opening of a number of sub-parallel fractures. Though the results are preliminary, our work clearly indicates that, when an accurate elastic Earth model is used, it is possible to fit the observations with volume and aperture changes that are essentially at the reservoir level, a depth of 1.8 km. That is, we do not require fluid movement to any depth significantly above the reservoir in order to fit the InSAR data.

Acknowledgments. Work performed at Lawrence Berkeley National Laboratory and Tele-Rilevamento Europa (TRE) was supported by the US Department of Energy under contract number DE-AC02-05- CH11231, Office of Basic Energy Sciences, and the GEOSEQ project for the Assistant Secretary for Fossil Energy, Office of Coal and Power Systems, through the National Energy Technology Laboratory of the US Department of Energy. The In Salah CO_2 Joint Industry Project (BP, StatoilHydro, and Sonatrach) is thanked for the provision and interpretation of production, injection, and subsurface data.

References

Arts, R., O. Eikan, A. Chadwick, P. Zweigel, L. van der Meer, and B. Zinszner (2004), Monitoring of CO_2 injected at Sleipner using time-lapse seismic data, *Energy* **29**, 1383-1392.

Alnes, H., O. Eiken, and T. Stenvold (2008), Monitoring gas production and CO_2 injection at the Sleipner field using time-lapse gravimetry, *Geophysics* **73**, WA155-WA161.

Baines, S. J., and R. H. Worden (2004), *Geological Storage of Carbon Dioxide* (eds Baines, S. J. & Worden, R. H.) 1-6, The Geological Society of London.

Burgmann, R., P. A. Rosen, and E. J. Fielding (2000), Synthetic aperture radar interferometry to measure Earth's surface topography and its deformation, *Annual Reviews of Earth and Planetary Sciences* **28**, 169-209.

Chang, E., D. S. Marx, M. A. Nelson, W. D. Gillespie, A. Putney, L. K. Warman, R. E. Chatham, and B. N. Barrett (2000), Long range active synthetic aperture sonar, results: Oceans 2000 Conference, Paper DTW-9901-00002, Providence R.I.

Chinnery, M. A., and D. B. Jovanovich (1972), Effect of Earth layering on earthquake displacement fields, *Bulletin of the Seismological Society of America* **62**, 1629-1639.

Davis, P. M. (1983), Surface deformation associated with a dipping hydrofracture, *Journal of Geophysical Research* **88**, 5826-5834.

Ferretti, A., C. Prati, and F. Rocca (2001), Permanent scatterers in SAR interferometry, *IEEE Transactions on Geoscience and Remote Sensing* **39**, 8-20.

Hansen, R. E., T. O. Saebo, H. J. Callow, and B. Langli (2006), The Sensotek interferometric synthetic aperture sonar: Results from Hugin AUV trials, Proceedings of the Eighth European Conference on Underwater Acoustics, Jesus, S. M. and O. C. Rodriguez (Eds.), Carvoeiro, Portugal.

Hearn, E. H., and R. Burgmann (2005), The effect of elastic layering on inversions of GPS data for coseismic slip and resulting stress changes: Strike-slip earthquakes, *Bulletin of the Seismological Society of America* **95**, 1637.

Hoversten, G. M., R. Gritto, J. Washbourne, and T. M. Daley (2003), Pressure and fluid saturation prediction in a multicomponent reservoir using combined seismic and electromagnetic imaging, *Geophysics* **68**, 1580-1591.

Lazaratos, S. K., and B. P. Marion (1997), Crosswell seismic imaging of reservoir changes caused by CO_2 injection, *The Leading Edge*, **16**, 1300-1306.

Massonnet, D., and K. L. Feigl (1998), Radar interferometry and its applications to changes in the Earth's surface, *Reviews of Geophysics* **36**, 441-500.

Ringrose, P., M. Atbi, D. Mason, M. Espinassous, O. Myhrer, M. Iding, A. Mathieson, and I. Wright (2009), Plume development around well KB-502 at the In Salah CO_2 storage site, *First Break* **27**, 1-5.

Savage, J. C. (1987), Effect of crustal layering upon dislocation modeling, *Journal of Geophysical Research* **92**, 10595-10600.

Schrag, D. P. (2007), Preparing to Capture Carbon, *Science* **315**, 812-813.

Vasco, D. W., K. Karasaki, and C. Doughty (2000), Using surface deformation to image reservoir dynamics, *Geophysics* **65**, 132-147.

Vasco, D. W., A. Ferretti, and F. Novali, F., (2008), Estimating permeability from quasi-static deformation: Temporal variations and arrival-time inversion, *Geophysics* **73**, O37-O52.

Wang, R., F. Lorenzo-Martin, and F. Roth (2006), PSGRN/PSCMP-a new code for calculating co- and post-seismic deformation, geoid and gravity changes based on the viscoelastic-gravitational dislocation theory, *Computers and Geosciences* **32**, 527-541.

White, D. J., G. Burrowes, T. Davis, Z. Hajnal, K. Hirsche, I. Hutcheon, E. Majer, B. Rostron, and S. Whittaker (2004), Greenhouse gas sequestration in abandoned oil reservoirs: The International Energy Agency Weyburn pilot project, *GSA Today* **14**, 4-10.

Zumberge, M., H. Alnes, O. Eiken, G. Sasagawa, and T. Stenvold (2008), Precision of seafloor gravity and pressure measurements for reservoir monitoring, *Geophysics* **73**, WA133-WA141.

6. Figure Captions

Figure 1. InSAR range velocity measurements, in mm/year, indicating the changes in distance between points on the surface of the Earth and a reference point in space. The three CO_2 injection wells (KB-501, KB-502, and KB-503) are labeled in this figure and their trajectories are indicated by the solid lines. The open circles denote the surface locations of the three wellheads. The cross, which signifies the origin of the local coordinate system, is located at longitude 2.137^o East and latitude 29.114^o North.

Figure 2. In Salah layered elastic model. (a) Compressional and shear velocity model for the In Salah region, derived from well logs. The upper and lower boundaries of the reservoir interval are indicated by the two horizontal lines.
(b) The range velocity at the surface due to the opening of a tensile crack at a depth of 1.8 km. The range velocity is shown for observation points situated along a line transverse to the plane of the tensile crack. The range velocity for a source within a homogeneous half-space (Uniform Moduli) is indicated by the filled squares. The crosses represent the range velocity for a source located within the 20 layer model shown in Figure 2a (Layered Moduli).

Figure 3. (a) Map view of the fractional volume change within the reservoir layer, obtained by an inversion of the range velocity observations. The location of well KB-502 is indicated by the open circle (well head) and the solid line. The northwest trending line represents the vertical fault/fracture suggested by seismic reflection data [*Ringrose et al.*, 2009]. The open rectangles situated along this line indicate the average aperture change along the fault/fracture. The size of each rectangle is proportional to the depth averaged aperture change at that point.
(b) The spatial distribution of aperture change over the vertical fault/fracture model produced by an inversion of the range velocity data. The upper and lower reservoir boundaries intersecting the fracture/fault plane are indicated by the two sub-parallel lines. The intersection of well KB-502 with the fault/fracture plane is indicated by the filled circle.

Figure 4. (a) Observed range velocities for the permanent scatterers surrounding well KB-502. The data in the lower left corner of the plot was influenced by fluid injection at well KB-503 and hence was not used in the inversion, it is blank in this figure. (b) Range velocities calculated using the model shown in Figure 3 and the forward modeling approach of *Wang et al.* [2006].

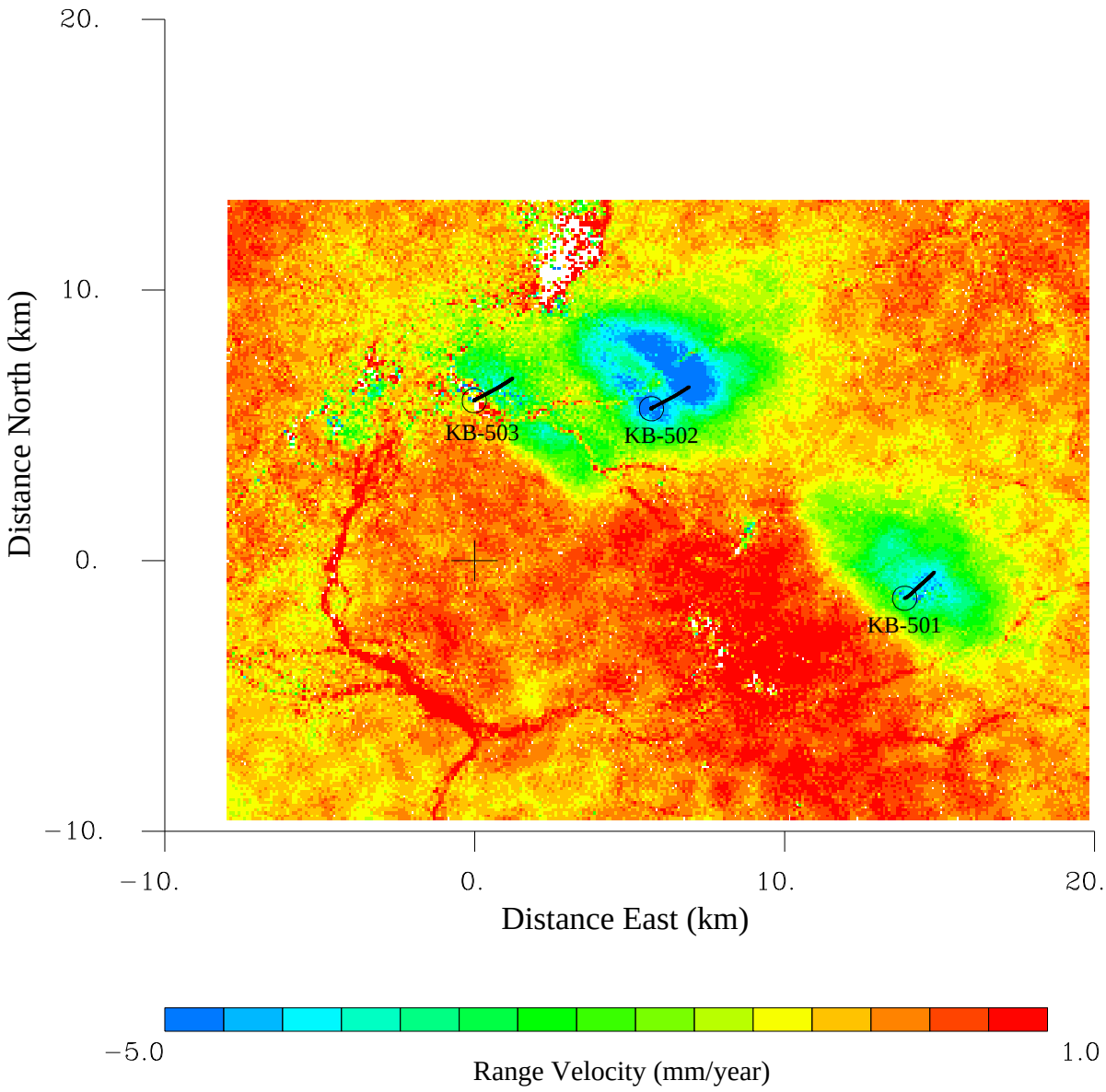
20.
10.
0.
−10.
Distance North (km)
KB-503
KB-502
KB-501
−10.
0.
10.
20.
Distance East (km)
−5.0
1.0
Range Velocity (mm/year)

Figure 1.

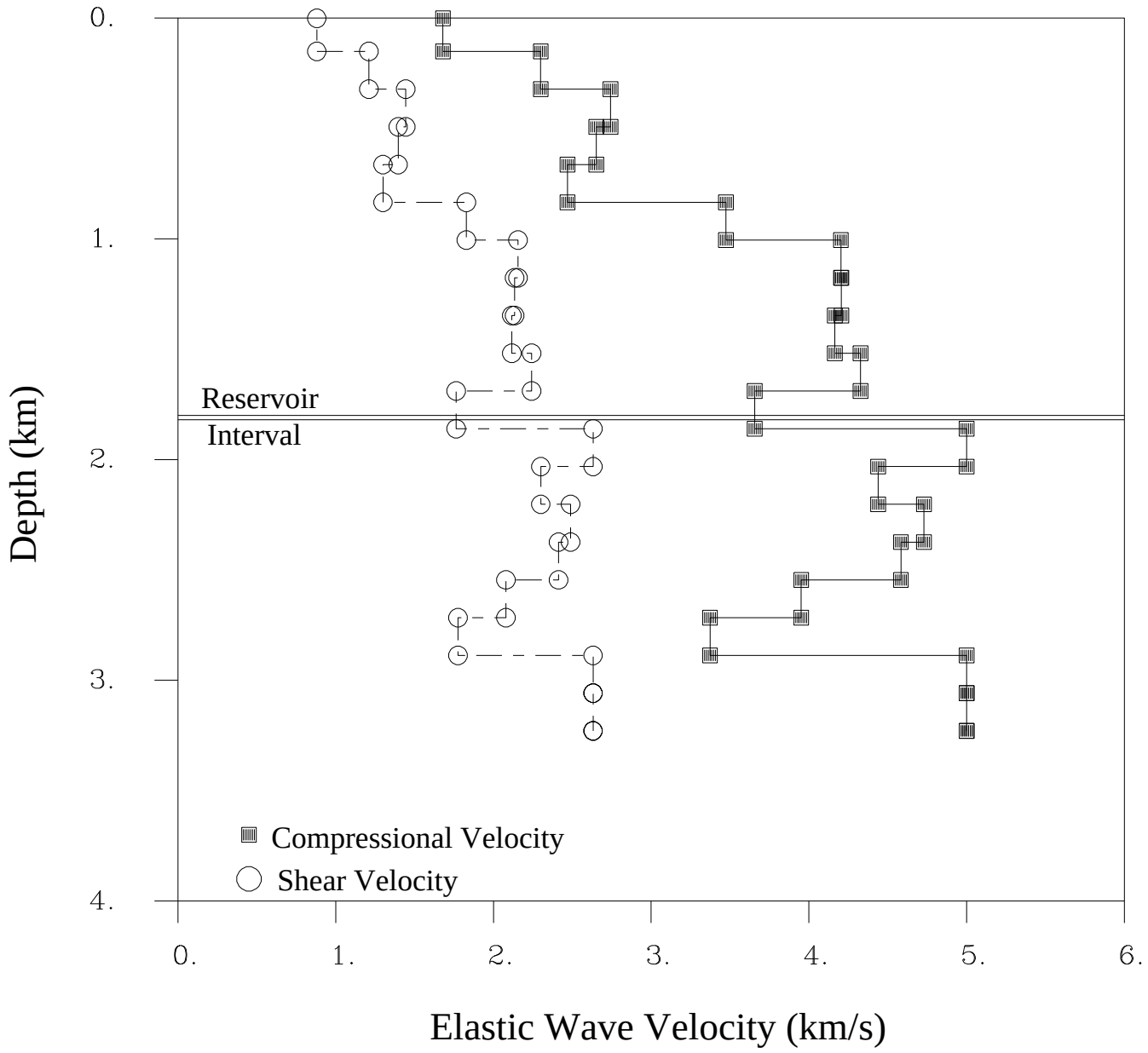
0.
1.
2.
3.
4.
Depth (km)
Reservoir
Interval
Compressional Velocity
Shear Velocity
0.
1.
2.
3.
4.
5.
6.
Elastic Wave Velocity (km/s)

Figure 2a.

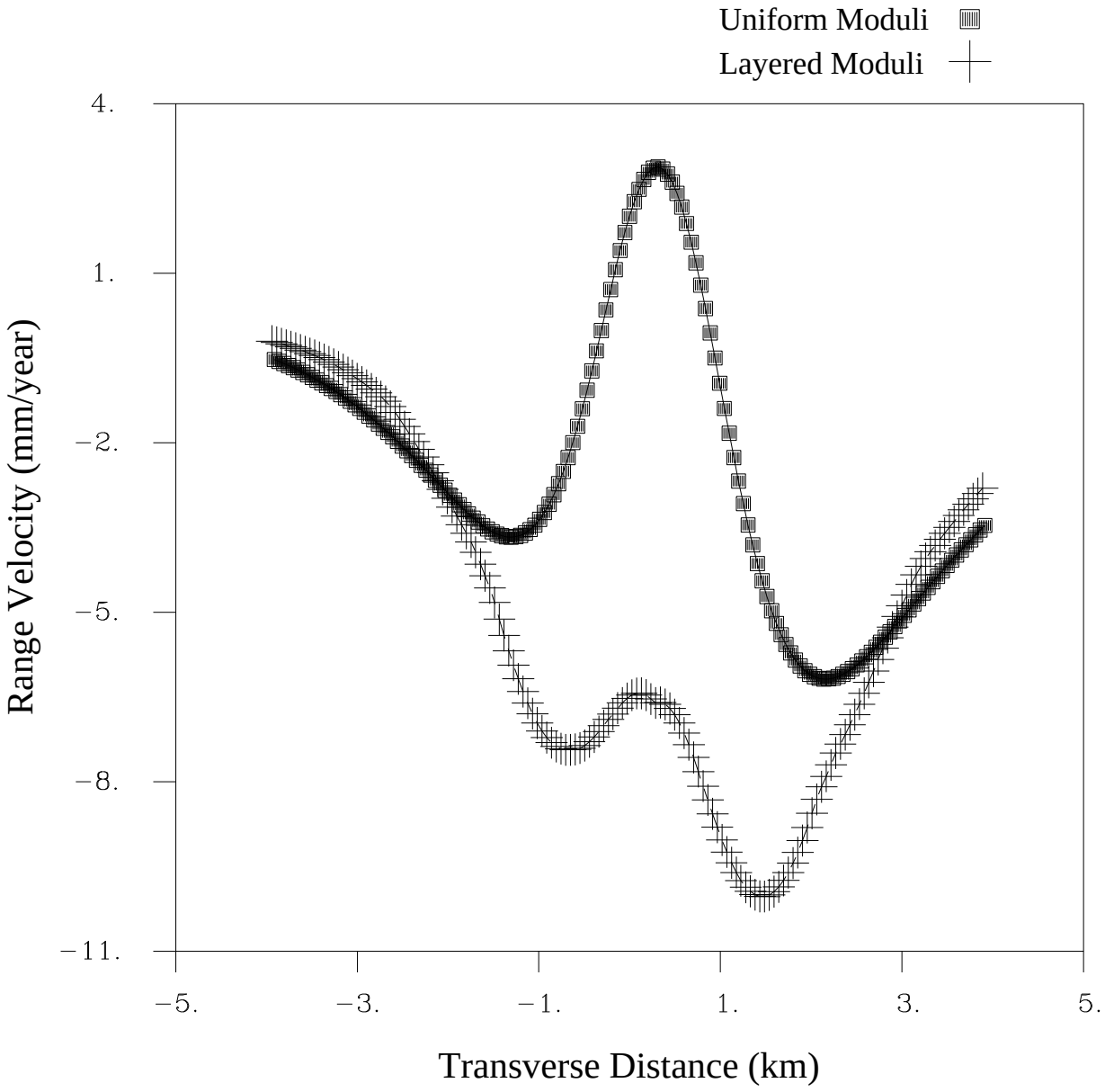
Uniform Moduli
Layered Moduli
4.
1.
−2.
−5.
−8.
−11.
Range Velocity (mm/year)
−5.
−3.
−1.
1.
3.
5.
Transverse Distance (km)

Figure 2b.

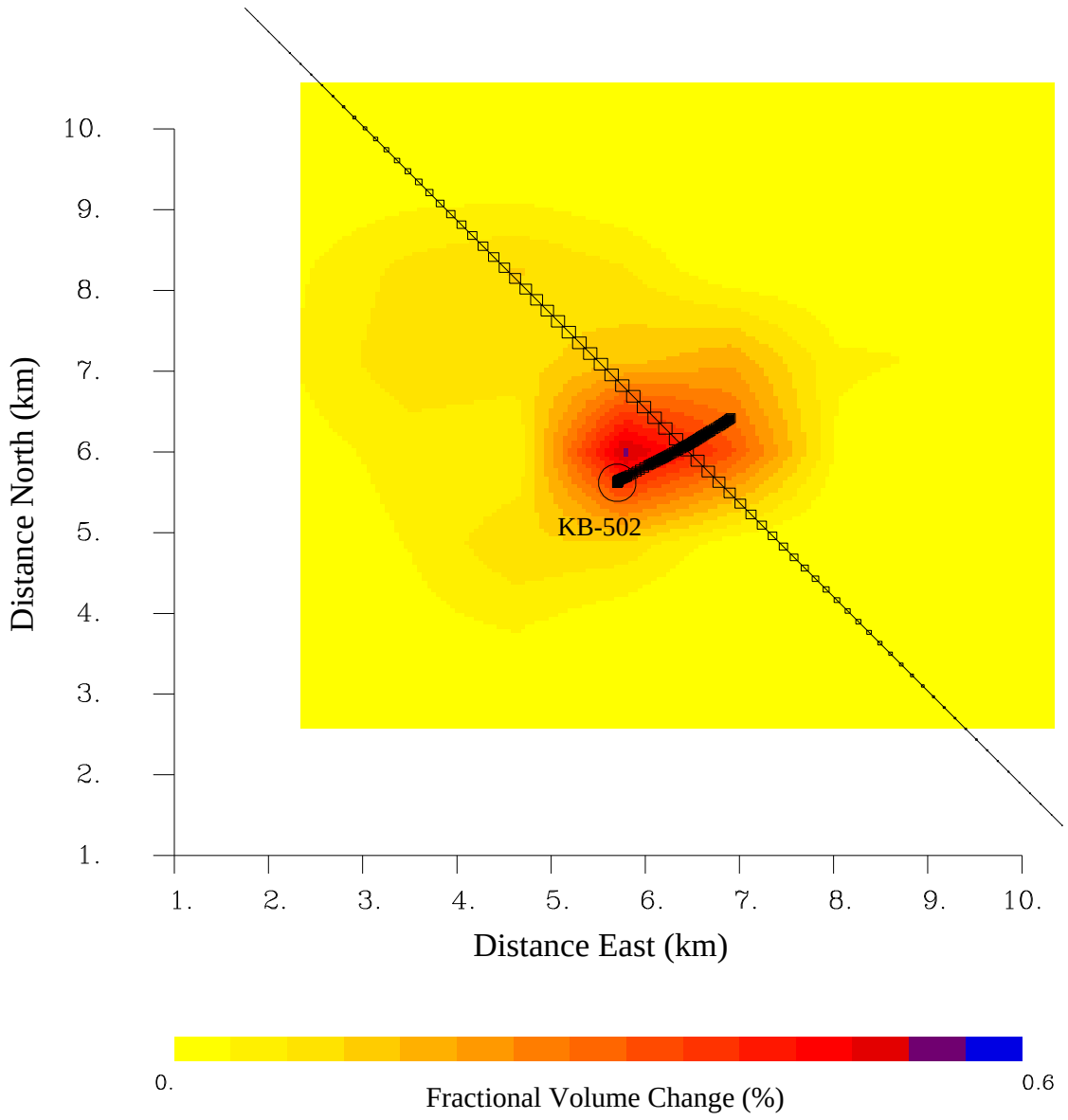
10.
9.
8.
7.
6.
5.
4.
3.
2.
1.
Distance North (km)
KB-502
1.
2.
3.
4.
5.
6.
7.
8.
9.
10.
Distance East (km)
0.
0.6
Fractional Volume Change (%)

Figure 3a.

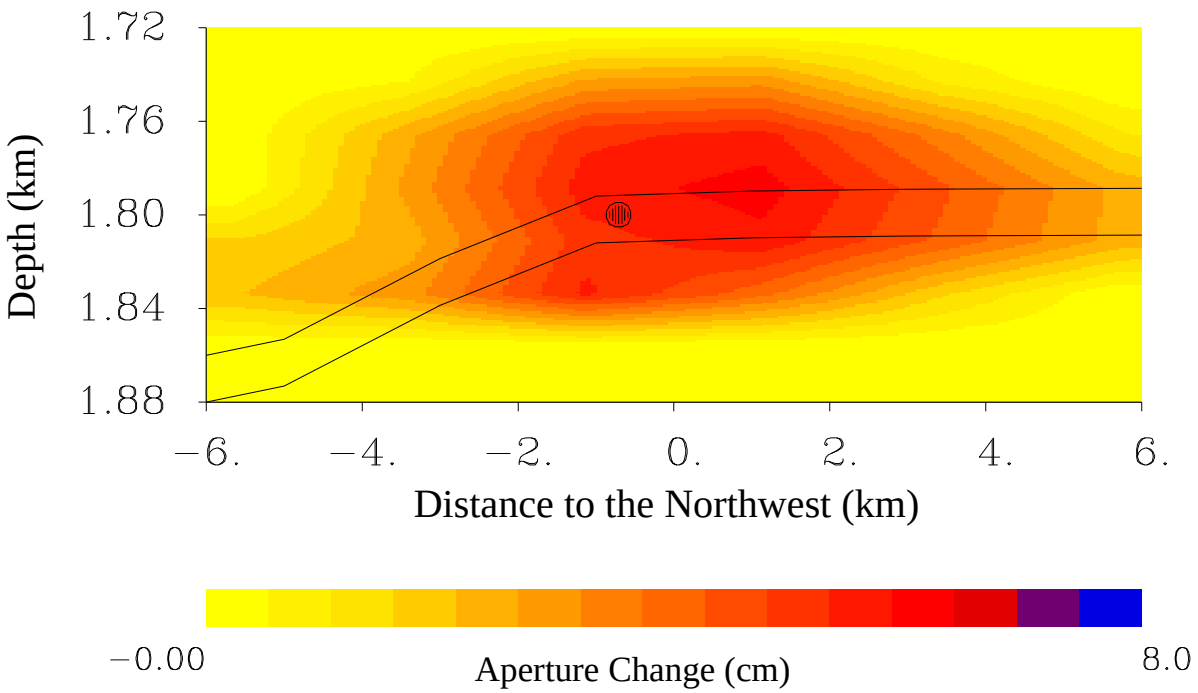
1.72
1.76
1.80
1.84
1.88
Depth (km)
−6.
−4.
−2.
0.
2.
4.
6.
Distance to the Northwest (km)
−0.00
Aperture Change (cm)
8.0

Figure 3b.

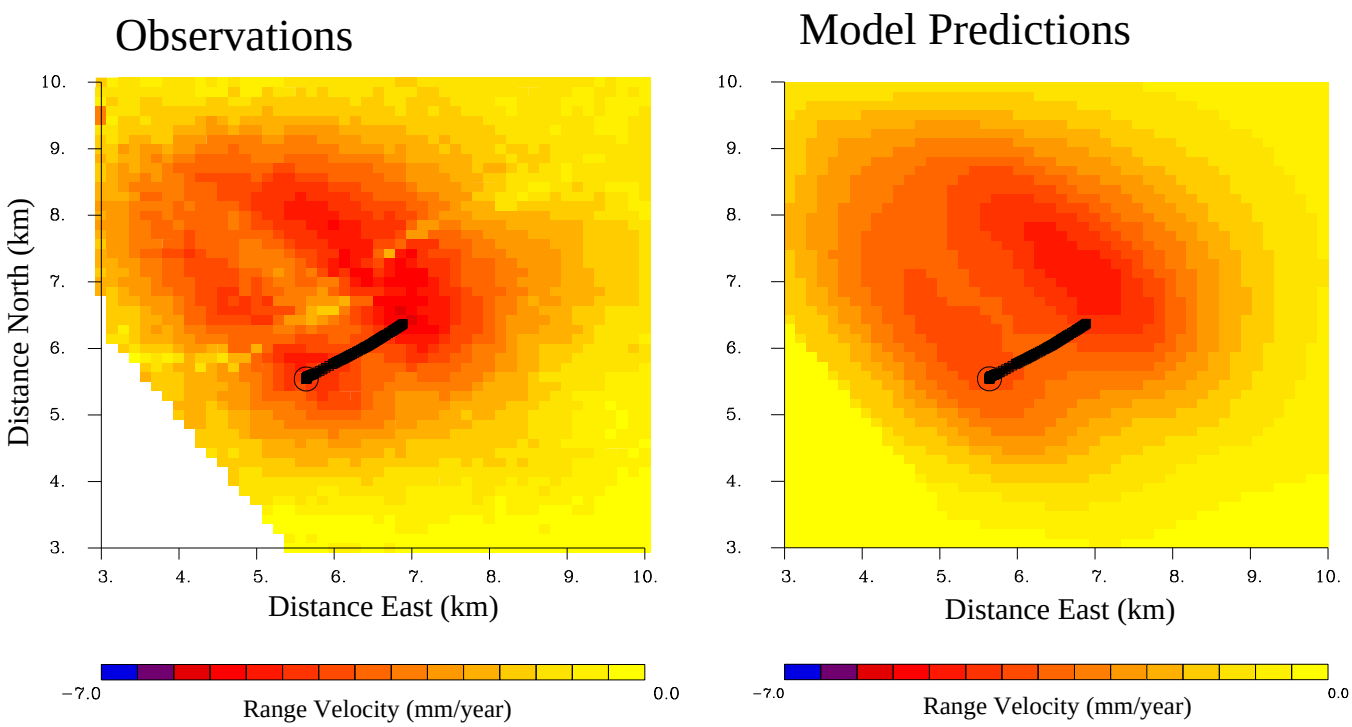
Observations
Model Predictions
Distance North (km)
Distance East (km)
Distance East (km)
Range Velocity (mm/year)
Range Velocity (mm/year)
−7.0
0.0
−7.0
0.0

Figure 4.